Development of very high luminance p-i-n junction-based blue fluorescent organic light-emitting diodes

*Yali Deng, Caroline Murawski, Changmin Keum, Kou Yoshida, Ifor D.W. Samuel, and Malte C. Gather**

Yali Deng, Dr. Caroline Murawski, Dr. Changmin Keum, Dr. Kou Yoshida, Prof. Ifor D.W. Samuel, Prof. Malte C. Gather
Organic Semiconductor Centre, SUPA, School of Physics and Astronomy, University of St Andrews, St Andrews, KY16 9SS, United Kingdom
E-mail: mcg6@st-andrews.ac.uk

Dr. Caroline Murawski
Kurt-Schwabe-Institut für Mess- und Sensortechnik e.V. Meinsberg, Kurt-Schwabe-Str. 4, 04736 Waldheim, Germany

Keywords: OLED, electron-blocking layer (EBL), device dimensions, resistance of anode contact, high current density, high brightness, CMOS

Abstract

Organic light-emitting diodes (OLEDs) can emit light over much larger areas than their inorganic counterparts, offer mechanical flexibility and can be readily integrated on various substrates and backplanes. However, the amount of light they emit per unit area is typically lower and the required operating voltage is higher, which can be a limitation for emerging applications of OLEDs, e.g. in outdoor and high-dynamic-range displays, biomedical devices or visible-light communication. Here, high-luminance, blue-emitting (λ_{peak} = 464 nm), fluorescent p-i-n OLEDs are developed by combining three strategies: Firstly, the thickness of the intrinsic layers in the device was decreased to reduced internal voltage loss. Secondly, different electron-blocking layer (EBL) materials were tested to recover efficiency losses resulting from this thickness reduction. Thirdly, the geometry of the anode contact was optimized, which led to a substantial reduction in the in-plane resistive voltage losses. OLEDs retain a maximum EQE of 4.4% as expected for an optimized fluorescent device and reach a luminance of 132,000 cd/m^2 and an optical power density of 2.4 mW/mm^2 at 5 V, a nearly 8-fold improvement compared to the original reference device.

1. Introduction

Starting with the milestone discovery by Tang and Van Slyke in 1987,[1] organic light-emitting diodes (OLEDs) have now been extensively studied for several decades. Today, OLED technology has reached maturity in display applications and sees initial use in solid-state lighting. OLEDs offer a unique combination of properties, in particular light weight, mechanical flexibility, ease of spectral tunability, rapid response, and compatibility with virtually any substrate – including silicon complementary metal-oxide semiconductor (CMOS) chips as well as flexible plastic and metal substrates. These properties have triggered an interest in using OLED technology beyond conventional display and lighting applications. However, in many cases, the lower luminance of OLEDs relative to e.g. inorganic GaN LEDs represents a challenge, in particular as the driving voltage available from CMOS chips is limited (often to 5 V).[2] Applications that would benefit from OLEDs with increased luminance include visible-light communication,[3,4] lasers,[5] or biomedical uses, e.g. in cancer treatment through photodynamic therapy,[6] sensors,[7,8] imaging,[9] and most recently optogenetics,[10–12] which is an emerging neuroscience technology that allows optical activation and silencing of genetically modified nerve cells with great specificity.[13,14] In many of these areas, the desired luminance is orders of magnitude higher than for displays and even general illumination. Optogenetics for example typically requires an irradiance of blue or red light in the mW/mm^2 range, which depending on the exact spectrum corresponds to a luminance of 50,000 to 500,000 cd/m^2.

One effective strategy for improving luminance is to increase the device quantum efficiency. Numerous researchers have focused on maximizing the internal quantum efficiency (IQE) of OLEDs, in particular by moving from fluorescent materials[15,16] to phosphorescent[17,18] and thermally activated delayed fluorescence (TADF) emitters.[19,20] Enhancing and balancing charge carrier injection and recombination has been equally important and is generally achieved through the use of OLED heterostructures, comprising hole- and electron-blocking layers (HBLs and EBLs) as well as hole- and electron-transport layers (HTLs and ETLs), the latter of which are often doped by molecular or metallic dopants.[21,22] In addition to improving the IQE of the device, such so-called p-i-n structures can also reduce the operating voltage and thus further increase power efficiency.[23,24] The reduction in voltage here is generally due to a combination of increased conductivity within the transport layers and reduced charge injection barriers at the interface between the transport layer and the adjacent electrode. Further improvements have been made through enhancing the efficiency of light extraction, often referred to as outcoupling efficiency, e.g. through integration of light scattering, microcavity

structures, refractive index coupling, and preferential orientation of the emissive molecules in the device.[25–27]

While the above strategies are helpful to enhance device luminance, a drastic increase in luminance relative to conventional OLED displays will also require increased current density. This brings a number of challenges: OLED structures based on phosphorescent or TADF emitters suffer from a strong efficiency roll-off with increasing current due to bimolecular quenching processes, in particular of triplet-triplet annihilation and triplet-polaron quenching[28] and in addition offer substantially slower response than fluorescent OLEDs. Joule heating and subsequent degradation may also be an issue, even though many applications do not require continuous operation at high luminance.[29] Several studies have reported that under pulsed operation conditions and through use of a small active area, OLEDs can sustain dramatically increased current densities.[30,31] Additionally, choosing a substrate with high thermal conductivity improves heat dissipation and thus prevents potential thermal breakdown.[32] However, management of Joule heating needs to be improved further to enable practical use of OLEDs in the applications discussed above.

In this work, we report high-luminance blue-emitting OLEDs by optimizing the charge blocking materials, the layer thickness in the device and the device dimensions. To minimize the impact of bimolecular quenching processes at high current density, we decided to use an emissive layer (EML) based on a fluorescent blue emitter. We first decreased the thickness of the intrinsic layers of a reference p-i-n OLED, which indicated that choosing a suitable EBL material is of particular importance. Testing a series of EBL materials with different charge mobilities and energy levels, led us to identify spiro-TAD as particularly well suited to our purpose. The current-voltage-luminance (*jVL*) characteristics were then investigated for devices with different physical dimensions. Due to the sheet resistance of the anode, we observed a strongly size-dependent *jV* relationship. For an optimized geometry, the current density and luminance were significantly improved, with the difference being more evident for some EBL materials than for others. To investigate this further, we sought to explore the intrinsic limit to current density by depositing OLEDs on thick and opaque metal anodes with negligible resistance. Based on our findings with opaque metal anodes, we further optimized the device geometry and achieved a maximum luminance of 132,000 cd/m^2 at 5 V. This corresponds to an 8-fold improvement in the optical power density compared to our starting device (from 0.3 to 2.4 mW/mm^2) while retaining a maximum EQE of 4.4%.

2. Results and discussion

2.1 Decreasing thickness of intrinsic layers

Figure 1a shows the structure of the reference p-i-n OLED used in this study, namely, indium tin oxide (ITO) anode (90 nm) / 2,2′,7,7′-tetrakis(*N*,*N*′-di-p-methylphenylamino)-9,9′-spirobifluorene (spiro-TTB) : 2,2′-(Perfluoronaphthalene-2,6-diylidene)dimalononitrile (F6-TNAP) (4 wt%, 40 nm) / *N*,*N*′-di(naphtalene-1-yl)-*N*,*N*′-diphenylbenzidine (NPB) (10 nm) / 2-methyl-9,10-bis(naphthalen-2-yl)anthracene (MADN) : 2,5,8,11-Tetra-tert-butylperylene (TBPe) (1.5 wt%, 20 nm) / bis-(2-methyl-8-chinolinolato)-(4-phenyl-phenolato)-aluminium(III) (BAlq) (10 nm) / 4,7-diphenyl-1,10-phenanthroline (BPhen) : Cs (3 wt%, 40 nm) / Al (100 nm). We have previously reported on the successful optogenetic control of locomotion in *Drosophila* larvae using an OLED with nearly identical structure.[33] Each device contained four pixels, each with an active area of 16.36 mm^2 and a blue electroluminescence (EL) spectrum (peak wavelength, 464 nm; Figure 1b). The *jVL* and external quantum efficiency (EQE) data in Figure 1c,d confirm that our devices reach relatively high luminance at low voltages, e.g. producing up to 16,000 cd/m^2 at 5 V.

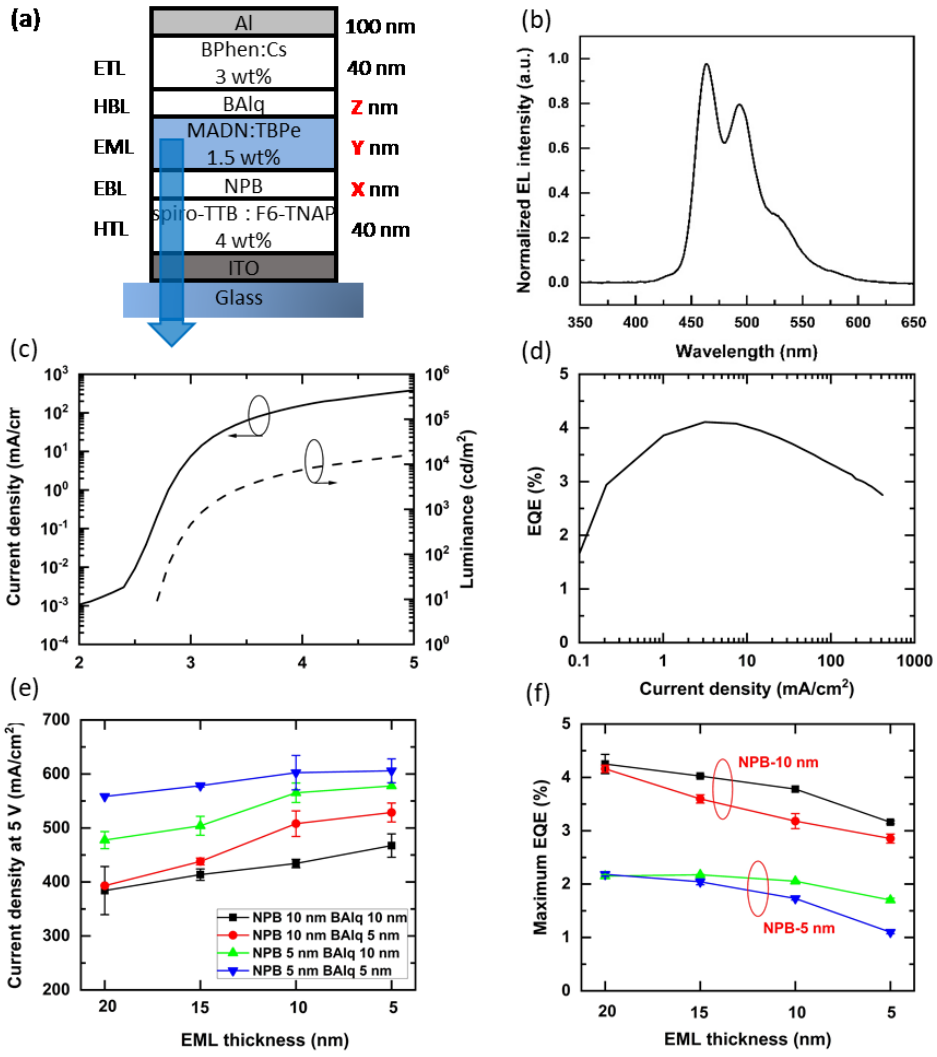

Figure 1. a) Schematic of the stack architecture of the OLEDs studied in this work. b) Electroluminescence spectrum, c) *jVL* and d) EQE for an OLED with thicknesses of X = 10 nm, Y = 20 nm, and Z = 10 nm. e) Summary of current density reached at 5 V and f) maximum EQE for OLEDs with different HBL, EBL, and EML thicknesses. Error bars show standard deviation from pixels.

Reducing the thickness of intrinsic layers in an OLED has been described as an attractive strategy to reduce the voltage drop across each layer and thus the resistance of the entire device.[34] First, we reduced the thickness of the EBL (here NPB) and HBL (here BAlq) from 10 nm to 5 nm and that of the EML (here MADN:TBPe) from 20 nm to 15, 10, and 5 nm. Figure 1e,f show the current density at 5 V and maximum EQE for the different thicknesses, showing a clear increase in current density with decreasing thickness of all intrinsic, undoped layers. The device with the thinnest layers (5 nm NPB, 5 nm BAlq, and 5 nm EML) exhibited

the highest current density (600 mA/cm^2 at 5 V), almost 1.6 times higher than that of the reference device which had the thickest intrinsic layers in this series (10 nm NPB, 10 nm BAlq, and 20 nm EML). However, for devices with reduced EML thickness, there was also a marked decrease in EQE. Decreasing the thickness of the EBL had an even more dramatic impact on the EQE; when the EBL thickness was reduced to 5 nm, the EQE dropped to approximately 1%, an almost 4-fold decrease compared to the reference device. By comparison, the thickness of the HBL did not have a substantial effect on the EQE. The EL spectra were not significantly affected by changing the thickness of the intrinsic layers. We concluded that the absolute change in total device thickness was too small to cause appreciable detuning to the weak micro-cavity formed by the metal cathode and the ITO anode of our OLEDs.

Overall, the blocking layers appear to play an important role in device performance, especially in terms of EQE when reducing the thickness of the EML. A high EQE can only be maintained if charges and excitons are well confined to the EML; otherwise, exciton diffusion away from the EML may lead to quenching, e.g. by F6-TNAP or Cs in the doped layers, while insufficient charge carrier blocking will lead to charge imbalance. For an ideal blocking layer, the EQE at low current density should be largely independent of the thickness of the EML.[35] One might also expect that the EML is hole-dominated and that excitons will therefore aggregate at the EML/HBL interface. However, the dependence of the EQE on EML and EBL thickness in our devices indicates insufficient electron blocking by the EBL material used (NPB), possibly as a result of an insufficient lowest unoccupied molecular orbital (LUMO) level. To investigate this further, we tested different EBL materials with higher LUMO values and good charge carrier mobility.

2.2 Optimizing EBL materials

Figure 2a shows the energy levels of the different EBL materials tested, alongside the energy levels of the other materials in our OLED stack. The HOMO and LUMO levels as well as the mobility of the different materials are also summarized in **Table 1**. Again, we investigated the effect of EML thicknesses on the device performance for each of the EBL materials; the resulting OLED stack architecture was as follows, ITO (90 nm) / spiro-TTB : F6-TNAP (4 wt%, 40 nm) / EBL (10 nm) / MADN : TBPe (1.5 wt%, X nm) / BAlq (10 nm) / BPhen : Cs (3 wt%, 40 nm) / Al (100 nm). As before, the current density significantly increases for all EBL materials when reducing the thickness of the EML (Figure 2b), which reflects the reduced

voltage drop across the EML. The device using α-NPD as EBL shows the lowest current density of all devices in this series, presumably due to the low charge mobility of this material (Table 1). At 5 V, the TAPC-based device shows the lowest EQE, which we attribute to a particularly high efficiency roll-off in these devices. The device using BF-DPB shows a comparable current density and EQE to the original NPB-based device. The device using spiro-TAD as the EBL shows the highest EQE and highest current density, indicating that this material offers the best combination of electron blocking, hole injection, hole-mobility and exciton confinement.

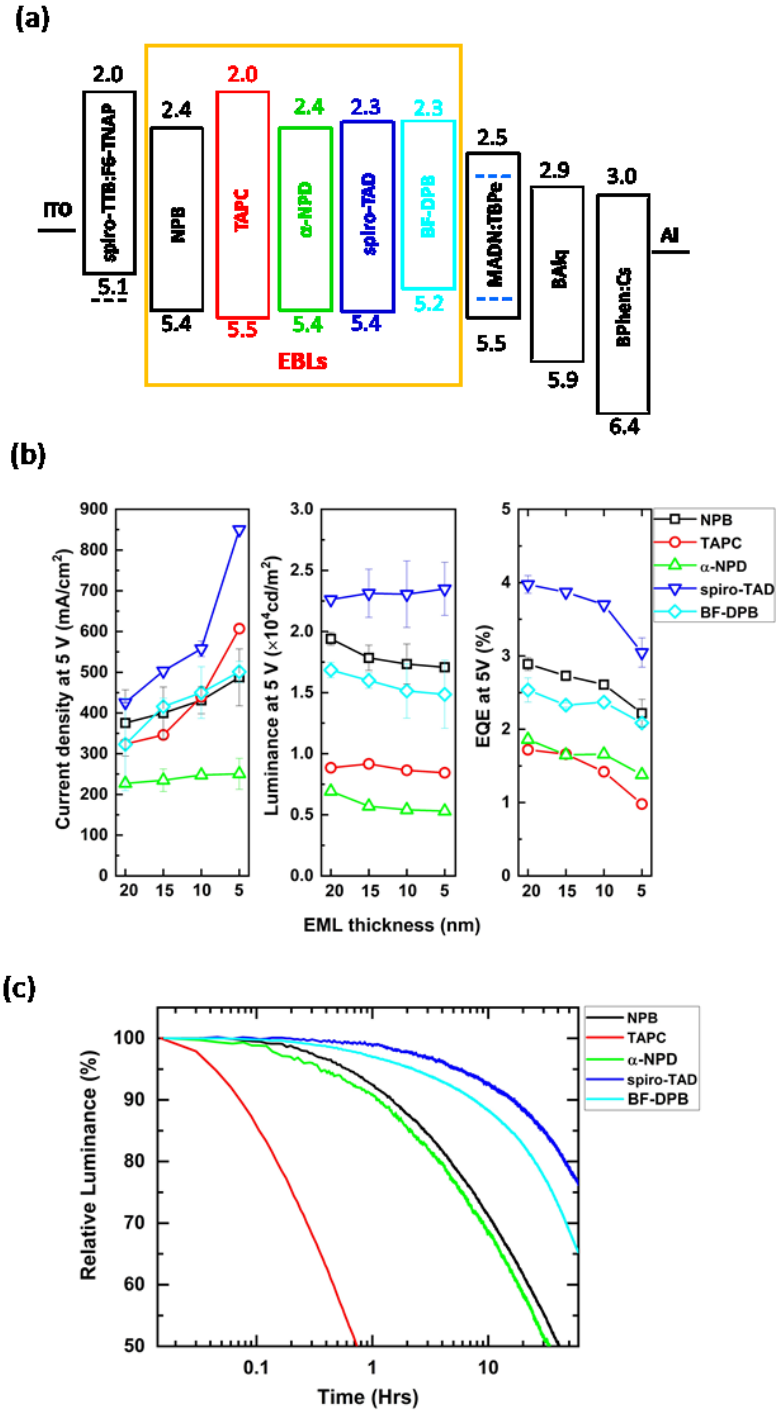

Figure 2. a) Energy level diagram of the OLED stack for the different EBL materials tested (indicated by yellow box). b) Current density, luminance and EQE of the OLEDs at 5 V for different EBL materials and different EML thicknesses (OLED active area, 16.36 mm^2, HBL and EBL thickness, 10 nm each). Symbols and error bars show average values and standard deviation for data taken from different OLEDs. c) Lifetime of OLEDs with different EBL materials at constant drive current of 44 mA/cm^2

and initial luminance of 1,400 – 3,100 cd/m^2, depending on EBL used. See Experimental Section for additional details.

Table 1. Summary of energy levels and charge carrier mobility for the different EBL materials tested in this study.

	NPB	TAPC	α-NPD	spiro-TAD	BF-DPB
HOMO (-eV)	**5.4**[39]	**5.5**[39]	**5.4**[40]	**5.4**[24]	**5.2**[43]
LUMO (-eV)	**2.4**	**2.0**	**2.4**	**2.3**	**2.3**
Mobility (cm^2/ (V s))	**2.2×10^{-4}**[39]	**2.4×10^{-3}**[39]	**1.8×10^{-4}**[41]	**3×10^{-4}**[42]	**5.7×10^{-5}**[43]

While the device EQE reduces slightly for thinner EMLs in all tested devices, this effect is not dramatic. Especially for spiro-TAD the drop in EQE is outweighed by the reduction in device resistance, thus allowing a net increase in device luminance at a given voltage for the thinner EML. At 5 V, the spiro-TAD-based OLED with the thinnest EML (5 nm) reaches a luminance of 23,500 cd/m^2 and a current density of 850 mA/cm^2 while maintaining an EQE of 3%. Therefore, the use of spiro-TAD allows a substantial increase in performance over the original reference device architecture, indicating that it is highly effective for blocking electrons and confining excitons.

Figure 2c compares the operational lifetime of OLEDs based on the different EBL materials tested here. In line with earlier literature reports on the intrinsic instability of the TAPC radical cation and the resulting poor stability of TAPC as hole-transport material,[36] TAPC-based OLEDs showed very short lifetime. However, the OLED using a spiro-TAD based EBL reached a t_{80} of 46 h under constant current drive at 44 mA/mm^2 and an initial luminance of 3,100 cd/m^2. Extrapolating this to initial luminance levels of 500 cd/m^2 and 1000 cd/m^2 with an acceleration factor of 2, yields t_{80} of 1800 h and 450 h, respectively. The good stability of the spiro-TAD based OLED is in agreement with literature demonstrating that spiro-linked compounds improve the morphological stability of the corresponding thin films.[37]

2.3 Adjusting electrode geometry

Next, we considered the resistance in the device electrodes and contact lines leading to each device to further improve the device current density. ITO is the most widely used anode material in OLEDs, in large part due to its high optical transparency and relatively good conductivity. However, compared to typical metal cathodes, e.g. made of aluminium, its sheet resistance R_s is orders of magnitude higher ($R_{s,\mathrm{ITO}} = 41.85\ \Omega/\square$ for the ITO anodes used in this study, while based on the bulk resistivity of aluminium one would expect $R_{s,\mathrm{Al}} = 0.3\ \Omega/\square$ for a 100 nm-thick Al cathode[38]).

Figure 3a shows a simplified schematic cross-section through our device. We first changed the size of the active device area by changing the length L_1 in the schematic, leaving the pixel width of 4 mm unchanged. Figure 3b shows a photograph of a device with 4 differently size active areas, ranging from roughly 16 mm^2 (same as for our reference device), to 8, 4, and 2 mm^2. For the device with the smallest area, Figure 3c,d show microscopic images of both the shadow mask used to define the device cathode and of the EL from the operating device. The images confirm that even for such a narrow pixel, the EL is homogenous across the device area, even though the active region is broadened by approximately 50 µm compared to the cathode mask. This broadening may result from a small gap between the cathode mask and the substrate during deposition of the cathode.

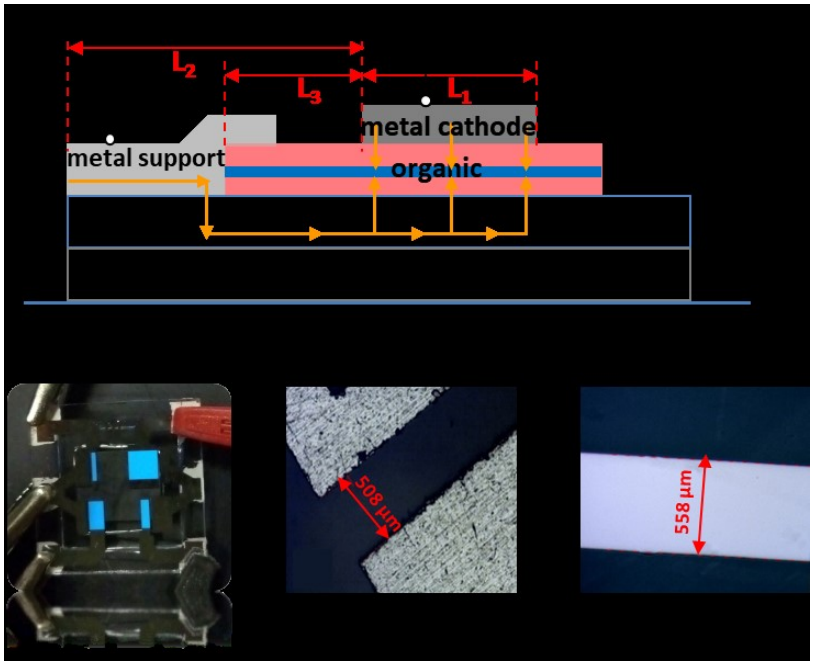

Figure 3. a) Simplified schematic of the critical dimensions of the OLEDs studied here. L_1 indicates the length of the active area of the device parallel to the direction of current in the anode contact, L_2 is the entire distance between the contact pad and the active pixel, and L_3 refers to the fraction of this

distance not covered by a metal support contact. b) Photograph of operating OLED with four active pixels with different dimensions. c) Microscope image of the slit in the shadow mask defining the narrowest of the four pixels in b. d) Microscope image of EL generated by the narrowest of the four pixels in b when driving the OLED.

Comparing the current density and luminance at 5 V for the different active areas and the different EBL materials (with 10 nm EBL/HBL and 5 nm EML) shows that both current density and luminance improve substantially when reducing the device active area, while there is no dramatic change in EQE (**Figure 4**a-c). The change in current density and luminance is particularly pronounced in the device with a spiro-TAD based EBL where a maximum current density and luminance of 2,900 mA/cm^2 and 76,000 cd/m^2, respectively, are achieved for an active area of 2 mm^2. The devices using NPB, BF-DPB, and TAPC as EBLs show comparable current densities, but the luminance of the TAPC-based device is much lower than for the other two devices due to its lower EQE. As before, the α-NPD-based device shows the lowest luminance because of its lower current density and EQE. Interestingly, the difference in device performance for different EBLs that was previously observed for the 16 mm^2 active area is even more pronounced for the smaller active areas. In addition, we found that the increase in current density and luminance with decreasing active area did not saturate, even for the smallest areas tested. Therefore, it seems likely that the resistance of the device electrodes is still limiting the overall current density and that additional optimization of device geometry can further increase the luminance reached at a given voltage.

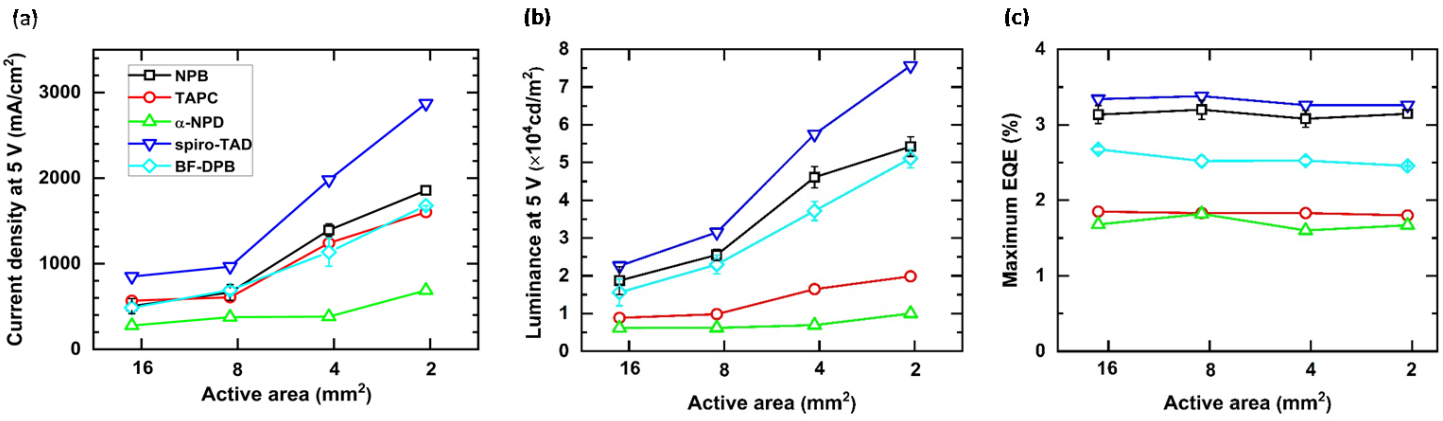

Figure 4. Summary of device characteristics of OLEDs with different active areas and different EBL materials; a) current density reached at 5 V, b) luminance reached at 5 V, and c) maximum EQE. Error bars show standard deviation from pixels.

2.4 Investigating the influence of anode resistance

The absolute resistance of an ITO anode or contact line is given by $R = R_{s,\mathrm{ITO}} \frac{L_i}{W_i}$, where L_i and W_i are the length and width of the i-th ITO section (compare Figure 3a); length is defined parallel to direction of current, width is perpendicular to the direction of current). In our case, the contact line (i.e. the distance between the contact pad and the pixel) has $\frac{L_2}{W_2} \approx 1.5$, however, as indicated in Figure 3a, most of the ITO contact line is covered by a thick aluminium layer. Thus, except for a remaining narrow gap L_3, resistance in the contact line is largely eliminated, leaving the resistance across the active ITO pixel as the dominant loss term.

To investigate the intrinsic resistance of the OLED stack, i.e. in the absence of any significant resistance from the electrodes, we replaced the transparent ITO contact by opaque aluminium layers of different thicknesses. While this renders the device mostly non-emissive and so ultimately not useful for practical applications, this strategy should provide insight into the maximum current density that can be achieved at a given voltage. The exact device structure was Al (X nm) / spiro-TTB : F6-TNAP (4 wt%, 40 nm) / spiro-TAD (10 nm) / MADN : TBPe (1.5 wt%, 20 nm) / BAlq (10 nm) / BPhen : Cs (3 wt%, 40 nm)/ Al (100 nm).

We first characterised the resistance of the different Al electrodes and of the reference ITO electrode by measuring current passing through a rectangular strip of electrode (**Figure 5**a). The sheet resistance decreases from $R_{s,\mathrm{Al}} = 16.92$ to 4.45, 2.28, and 1.59 Ω/□ as the thickness increases from 10 nm to 30, 60, and 100 nm, respectively. The ITO has $R_{s,\mathrm{ITO}} = 41.85$ Ω/□ as stated above.

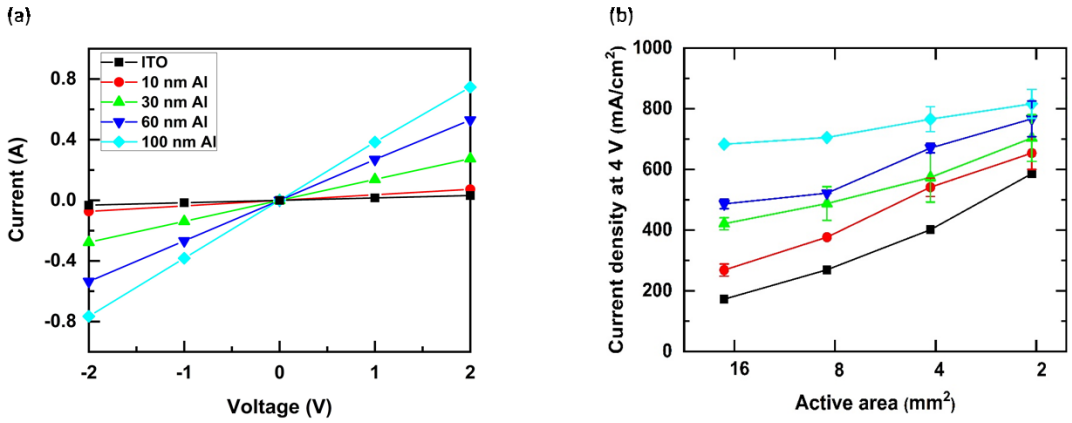

Figure 5. a) Resistance measurement of Al bottom electrodes with different thickness and of the ITO reference electrode. All electrodes have the same rectangular shape with length of 13 mm and width of 4 mm. b) Comparison of current density (with standard deviation) at 4 V reached in OLEDs with different active areas and different bottom electrodes, using spiro-TAD as EBL.

Figure 5b summarizes the OLED current density reached at a drive voltage of 4 V, comparing the different aluminium thicknesses and active areas and also showing the ITO anode for comparison. For the thinner aluminium layers (10, 30 and 60 nm) the trend is similar to the ITO electrode, i.e. a substantial increase in current density for smaller active area. However, the absolute current is significantly larger than in the ITO device, especially for aluminium layers thicker than 30 nm. For the 100 nm thick aluminium electrode, the current density is nearly identical for all device areas tested, indicating that electrode resistance is no longer the limiting factor to current density in this device. As the device active area is reduced, the current density reached in the different devices converges toward a common value, suggesting that for very small active areas the measured current density is dominated by the intrinsic resistance of the OLED stack. Overall, the maximum current density achieved at 4 V is ~ 800 mA/cm^2; this is achieved for the smallest pixel (2 mm^2) and thickest aluminium layer (100 nm). At 2 mm^2 active area, even the ITO anode-based device already reaches 72% of this current density.

To access the remaining potential for increase in current density, we sought to further reduce L_3, the length of the ITO contact line between the reinforced aluminium contact and the edge of the active area of the OLED as this should allow a further reduction in the voltage drop on the anode side. By careful design of the shadow masks used for deposition of the organic

material and aluminium contacts, it was possible to reduce L_3 to 0.5 mm, thus yielding $\frac{L_3}{W_3} \approx 0.125$ without adding additional complexity to the fabrication process.

For the final device generation, we returned to an EML thickness of 20 nm as reducing the EML thickness to 5 nm led to a 25% reduction in EQE and only yielded a modest increase in luminance compared to the other improvements made in this work. **Figure 6**a,b compare the *jVL* characteristics and EQE achieved for this final iteration to the other device generations of this study. Interestingly, for OLEDs with a spiro-TAD based HBL the EQE roll-off appears to become slower at current densities above 1 A/cm^2. One possible explanation is that the width of the emission zone in these devices may increase at high current densities. In previous work, we have modelled the roll-off behaviour of OLEDs and found that the EQE roll-off characteristics become skewed if the emission zone broadens with increasing current density.[28] Comparing the different generations of devices reveals a steady increase in current density and luminance due to the reduction of the device active area from 16 mm^2 to 2 mm^2 (reduction in L_1), the exchange of NPB for spiro-TAD as the EBL material, and the reduction of contact line (reduction in L_3). Combined, these measures yielded a device with luminance of 132,000 cd/m^2, current density of 3,000 mA/cm^2 when driven at 5 V and a maximum EQE of 4.4%. Using the EL spectrum of the final devices, we converted the luminance into optical power density emitted by the different OLEDs (i.e. the "radiant exitance" of each device). The best device reaches an optical power density of 2.4 mW/mm^2, a nearly 8-fold improvement compared to our original reference device (Figure 6c).

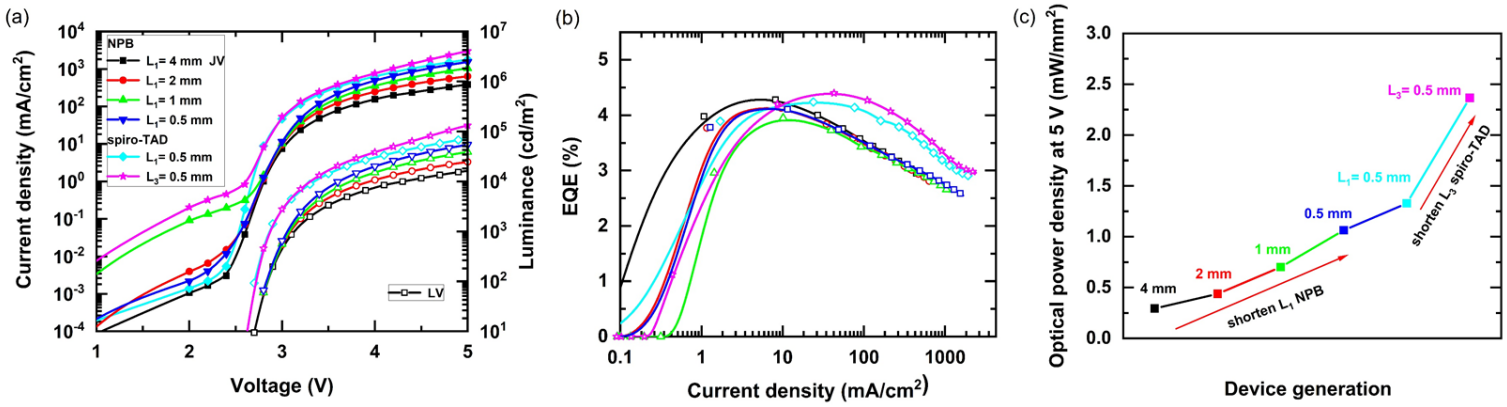

Figure 6. Comparison of a) *jVL* characteristics and b) EQE of the different devices tested in this study, comparing the original EBL material (NPB) and the best-suited EBL material (spiro-TAD) and the

different device dimensions. c) Summary of the optical power density emitted by the devices from the different generations.

3. Conclusion

In this study, we identified the thickness of each intrinsic layer (HBL, EML, and EBL) as a key variable that requires very careful optimization. The properties of different electron blocking materials turned out to be of particular importance for thinner EMLs. Furthermore, we showed that the resistance on the anode contact plays a crucial role when OLEDs are operated in a high current and high luminance regime. Through re-design of the shadow masks used during deposition of the different layers, we were able to adjust the critical dimensions of the device and thus nearly eliminate the parasitic resistance from the device electrodes. Our shadow mask process avoids the potential difficulties resulting from a more complex lithography-based fabrication process.

Our final devices maintained a maximum EQE of 4.4%, in line with the expectation for optically optimized fluorescent OLEDs. Importantly, they reached a current density and luminance at 5 V drive voltage of 3,000 mA/cm^2 and 132,000 cd/m^2, respectively, which corresponds to an improvement in optical power density from 0.3 to 2.4 mW/mm^2. To our knowledge, this represents the highest optical power density reached by a blue OLED driven at CMOS compatible voltage levels to date. We expect the achievement of such high luminance at low voltage to open new fields of application of OLEDs.

4. Experimental Section

All OLEDs were fabricated on pre-patterned ITO substrates with a thickness of ~ 90 nm which were sequentially cleaned in ultrasonic baths with acetone and isopropanol. The substrates were dried with a nitrogen gas gun, followed by ultraviolet ozone plasma treatment (3 min), and then placed into an evaporator chamber for high-vacuum thermal evaporation (at a base pressure of approximately 10^{-7} mbar). Evaporation rates were controlled by the heating power and monitored by a quartz crystal monitor. Different shadow masks were used for the deposition of the organic layers and the metal electrode to define the structure and geometry of the active area. All organic materials were purchased from Lumtec at the highest available purity grade and used without further purification.

After thermal evaporation, devices were transferred from the vacuum chamber into a nitrogen-filled glovebox without intermittent exposure to air and then encapsulated with getter-embedded cavity glass lids attached by a UV-curable epoxy glue.

jVL characteristics were measured with a source meter (Keithley 2400) and a calibrated Si-photodiode connected to a multimeter (Keithley 2000). EL spectra were recorded by a spectrograph (MS125, Oriel) connected to a charge-coupled device (CCD) camera (Andor DV420-BU). Lifetime measurements were performed with a dedicated multi-channel OLED Lifetime Test System (McScience M6000PMX). All the measurements were carried out at room temperature under ambient conditions and in steady state.

EBL materials used in this study are: *N*,*N*′-di(naphtalene-1-yl)-*N*,*N*′-diphenylbenzidine (NPB); di-[4-(*N*,*N*-di-p-tolyl-amino)-phenyl]cyclohexane (TAPC); *N*,*N*′-bis(naphthalen-1-yl)-*N*,*N*′-bis(phenyl)-2,2′-dimethylbenzidine (α-NPD); 2,2′,7,7′-tetrakis(*N*,*N*-diphenylamino)-2,7-diamino-9,9-spirobifluorene (spiro-TAD); *N*4,*N*4′-bis(9,9-dimethyl-9H -fluoren-2-yl)-*N*4,*N*4′-diphenylbiphenyl-4,4′-diamine (BF-DPB).

Precise device active areas and length L_1 are: 16.36 mm^2 (L_1 = 4.07 mm), 8.35 mm^2 (L_1 = 2.08 mm), 4.33 mm^2 (L_1 = 1.08 mm), 2.29 mm^2 (L_1 = 0.57 mm). The precise width of pixels is W = 4.02 mm.

For the OLED lifetime measurements shown in Fig. 2c, the device area was 2.29 mm^2. EBL / EML / HBL thicknesses were 10 nm / 20 nm / 10 nm for all devices except for the OLED with an α-NPD based EBL, where thicknesses were 5 nm / 20 nm / 5 nm, and the OLED with a BF-DPB based EBL, where thicknesses were 10 nm / 5 nm / 10 nm.

References

[1] C. W. Tang and S. A. VanSlyke, *Appl. Phys. Lett.* **1987**, 51, 913.

[2] H. Ballan, M. Declercq, *High Voltage Devices and Circuits in Standard CMOS Technologie*s, Springer Science & Business Media, **2013**.

[3] M. T. Sajjad, P. P. Manousiadis, C. Orofino, A. L. Kanibolotsky, N. J. Findlay, S. Rajbhandari, D. A. Vithanage, H. Chun, G. E. Faulkner, D. C. O'Brien, P. J. Skabara, G. A. Turnbull, I. D. W. Samuel, *Appl. Phys. Lett.* **2017**, 110, 013302.

[4] H. Chen, Z. Xu, Q. Gao, S. Li , *IEEE Photonics Journal* **2018**, 10, 7901312.

[5] A. S. D. Sandanayaka, T. Matsushima, F. Bencheikh, S. Terakawa, W. J. Potscavage, C. Qin, T. Fujihara, K. Goushi, J. C. Ribierre, C. Adachi, *Appl. Phys. Express.* **2019**, 12, 061010.

[6] S. K. Attili, A. Lesar, A. McNeill, M. Camacho-Lopez, H. Moseley, S. Ibbotson, I. D. W. Samuel and J. Ferguson, *Br. J. Dermatol.* **2009**, 161, 170.

[7] A. K. Bansal, S. Hou, O. Kulyk, E. M. Bowman, I. D. W. Samuel, *Adv. Mater.* **2015**, 27, 7638.

[8] M. Ramuz, L. Bürgi, R. Stanley, C. Winnewisser, *J. Appl. Phys.* **2009**, 105, 084508.

[9] C. Murawski, A. Mischok, J. Booth, J. D. Kumar, E. Archer, L. Tropf, C. M. Keum, Y. L. Deng, K. Yoshida, I. D. W. Samuel, M. Schubert, S. R. Pulver, M. C. Gather*, *Adv. Mater.* **2019**, 1903599.

[10] A. Steude, M. Jahnel, M. Thomschke, M. Schober, M. C. Gather, *Adv. Mater.* **2015**, 27, 7657.

[11] A. Morton, C. Murawski, Y. Deng, C. Keum, G. B. Miles, J. A. Tello, M. C. Gather, *Adv. Biosys.* **2019**, 3, 1800290.

[12] J. T. Smith, B. O'Brien, Y. K. Lee, E. J. Bawolek, J. B. Christen, *IEEE/OSA J. Disp. Technol.* **2014**, 10, 514.

[13] L. Fenno, O. Yizhar, K. Deisseroth, *Annu. Rev. Neurosci.* **2011**, 34, 389.

[14] E. Pastrana, *Nat. Methods.* **2011**, 8, 24.

[15] M. Zhu and C. Yang, *Chem. Soc. Rev.* **2013**, 42, 4963.

[16] K. H. Kim, J. Y. Baek, C. W. Cheon, C. K. Moon, B. Sim, M. Y. Choi, J. J. Kim and Y. H. Kim, *Chem. Commun.* **2016**, 52, 10956.

[17] J. Lee, H. F. Chen, T. Batagoda, C. Coburn, P. I. Djurovich, M. E. Thompson, S. R. Forrest, *Nat. Mater.* **2015**, 15, 92.

[18] Z. Q. Zhu, K. Klimes, S. Holloway, J. Li, *Adv. Mater.* **2017**, 29, 1605002.

[19] H. Uoyama, K. Goushi, K. Shizu, H. Nomura, C. Adachi, *Nature* **2012**, 492, 234.

[20] S. Hirata, Y. Sakai, K. Masui, H. Tanaka, S. Y. Lee, H. Nomura, N. Nakamura, M. Yasumatsu, H. Nakanotani, Q. Zhang, K. Shizu, H. Miyazaki, C. Adachi, *Nat. Mater.* **2015**, 14, 330.

[21] S. Reineke, F. Lindner, G. Schwartz, N. Seidler, K. Walzer, B. Lüssem, K. Leo, *Nature* **2009**, 459, 234.

[22] B. Lüssem, M. Riede, K. Leo, *Phys. Status Solidi A* **2013**, 210, 9.

[23] G. He, O. Schneider, D. Qin, X. Zhou, M. Pfeiffer, K. Leo, *J. Appl. Phys.* **2004**, 95, 5773.

[24] Y. Duan, M. Mazzeo, V. Maiorano, F. Mariano, D. Qin, R. Cingolani, G. Gigli, *Appl. Phys. Lett.* **2008**, 92, 113304.

[25] M. C. Gather, S. Reineke, *J. Photonics Energy.* **2015**, 5, 057607.

[26] H. W. Chang, J. Lee, S. Hofmann, Y. Hyun Kim, L. Müller-Meskamp, B. Lüssem, C. C. Wu, K. Leo, M. C. Gather, *J. Appl. Phys.* **2013**, 113, 204502.

[27] J. Song, K. H. Kim, E. Kim, C. K. Moon, Y. H. Kim, J. J. Kim, S. Yoo, *Nat. Commun.* **2018**, 9, 3207.

[28] C. Murawski, K. Leo, M. C. Gather, *Adv. Mater.* **2013**, 25, 6801.

[29] A. Fischer, T. Koprucki, K. Gärtner, M. L. Tietze, J. Brückner, B. Lüssem, K. Leo, A. Glitzky, R. Scholz, *Adv. Funct. Mater.* **2014**, 24, 3367.

[30] D. Kasemann, R. Brückner, H. Fröb, K. Leo, *Phys. Rev. B.* **2011**, 84, 115208.

[31] K. Hayashi, H. Nakanotani, M. Inoue, K. Yoshida, O. Mikhnenko, T. Q. Nguyen, and C. Adachi, *Appl. Phys. Lett.* **2015**, 106, 093301.

[32] K. Yoshida, H. Nakanotani, C. Adachi, *Org. Electron.* **2016**, 31, 287.

[33] A. Morton, C. Murawski, S. R. Pulver, M. C. Gather, *Sci. Rep.* **2016**, 6, 31117.

[34] Y. Zhao, J. Chen, D. Ma, *Appl. Phys. Lett.* **2011**, 99, 163303.

[35] G. He, O. Schneider, D. Qin, X. Zhou, M. Pfeiffer, K. Leo, G. He, O. Schneider, D. Qin, X. Zhou, M. Pfeiffer, K. Leo, *J. Appl. Phys.* **2004**, 95, 5773.

[36] S. Dong, L. Xu, C. W. Tang, *Org. Electron.* **2017**, 42, 379.

[37] T. P. I. Saragi, T. Fuhrmann-Lieker, and J. Salbeck, *Adv. Funct. Mater*. 2006, 16, 966.

[38] R. A. Serway, *Principles of Physics,* Fort Worth Saunders College Pub. **1998**, p. 602.

[39] C. Kulshreshtha, J. W. Choi, J. K. Kim, W. S. Jeon, M. C. Suh, Y. Park, J. H. Kwon, *Appl. Phys. Lett.* **2011**, 99, 023308.

[40] H. Lee, J. Kwak, C. M. Kang, Y. Y. Lyu, K. Char, C. Lee, *Opt. Express.* **2015**, 23, 11424.

[41] N. D. Nguyen and M. Schmeits, *Phys. Rev. B* **2007**, 75, 075307.

[42] D. C. Neckers, G. Bünau, W. S. Jenks, *Advances in Photochemistry*, John Wiley & Sons Inc. **2002**, p. 140.

[43] T. Menkea, D. Ray, H. Kleemanna, M. P. Hein, K. Leo, M. Riede, *Org. Electron.* **2014**, 15, 365.

Acknowledgements

This research was financially supported by the EPSRC NSF-CBET lead agency agreement (EP/R010595/1, 1706207), the DARPA-NESD programme (N66001-17-C-4012) and the Leverhulme Trust (RPG-2017-231). Y. L. D. acknowledges a stipend from the Chinese Scholarship Council (CSC). C. M. acknowledges funding by the European Commission through a Marie Skłodowska Curie Individual Fellowship (703387). Diese Arbeit wurde mitfinanziert durch Steuermittel auf der Grundlage des vom Sächsischen Landtag beschlossenen Haushaltes. C. M. K. acknowledges support from the Basic Science Research Program through the National Research Foundation of Korea (NRF) funded by the Ministry of Education (2017R1A6A3A03012331).

Conflict of Interest

The authors declare no conflict of interest.

Table of contents entry:

Blue organic light-emitting diodes (OLEDs) with extremely high brightness at CMOS compatible drive voltages are developed. Optimization of charge blocking layers and geometry enables a luminance exceeding 100,000 cd/m^2 at 5 V, which corresponds to an optical power density at the device surface of 2.4 mW/mm^2. This opens opportunities for monolithic integration of OLEDs on CMOS chips, e.g. for bioimplants.

Keyword: OLED, electron-blocking layer (EBL), device dimensions, resistance of anode contact, high current density, high brightness, CMOS

Development of very high luminance p-i-n junction-based blue fluorescent organic light-emitting diodes

*Yali Deng, Caroline Murawski, Changmin Keum, Kou Yoshida, Ifor D.W. Samuel, and Malte C. Gather**